


# Calculation of third to eighth virial coefficients of hard lenses and hard, oblate ellipsoids of revolution employing an efficient algorithm

Philipp Marienhagen<sup>1</sup>, Robert Hellmann<sup>2</sup>, and Joachim Wagner<sup>1,\*</sup>

<sup>1</sup>Institut für Chemie, Universität Rostock, Albert-Einstein-Straße 3a, 18059 Rostock, Germany

<sup>2</sup>Institut für Thermodynamik, Helmut-Schmidt-Universität/Universität der Bundeswehr Hamburg, 22043 Hamburg, Germany

 (Received 21 May 2021; accepted 25 June 2021; published 19 July 2021)

We provide third to eighth virial coefficients of oblate, hard ellipsoids of revolution and hard lenses in dependence on their aspect ratio  $\nu$ . Employing an algorithm optimized for hard anisotropic shapes, highly accurate data are accessible with comparatively small numerical effort. For both geometries, reduced virial coefficients  $\tilde{B}_i(\nu) = B_i(\nu)/B_2^{i-1}(\nu)$  are in first approximation proportional to the inverse excess contribution  $\alpha^{-1}$  of their excluded volume. The latter quantity is directly accessible from second virial coefficients and analytically known for convex bodies.

DOI: [10.1103/PhysRevE.104.015308](https://doi.org/10.1103/PhysRevE.104.015308)

## I. INTRODUCTION

Starting with the seminal work of Onsager [1], hard anisotropic solids attracted increasing interest as a model system for condensed matter, where a competition of entropy resulting from rotational and translational degrees of freedom determines the equation of state and therewith the phase behavior of such systems.

An obvious route to extend the spherically symmetric hard sphere model to anisotropic particles is the affine transformation to ellipsoids. In the special case of axial symmetry, ellipsoids of revolution are obtained with tunable aspect ratio  $\nu$  as a single parameter of anisometry. Such systems are thoroughly investigated as model systems for liquid crystalline matter [2–5]. The influence of the detailed particle shape becomes evident comparing the phase behavior of ellipsoids and hard spherocylinders [6–8]. While ellipsoids and spherocylinders are continuous with respect to their surface curvature, lenses possess a two-dimensional discontinuity at their equators. The impact of such discontinuities to second virial coefficients is known [9]. Recently, the phase behavior of hard lenses has been investigated [10–12].

Much earlier, van der Waals [13], Jäger [14], and Boltzmann [15,16] used the excluded volume to calculate the virial coefficients of hard spheres up to order 4. Kamerlingh Onnes [17] proposed the virial series as an equation of state for gases and liquids, where orientational degrees of freedom average out. The fifth- and higher-order virial coefficients became accessible with emerging computer simulation techniques [18–20].

Using Monte Carlo methods and numerical approaches for the contact function of anisotropic hard solids, also third- and higher-order virial coefficients of such systems became available. In addition to spherocylinders [21,22], the virial coefficients of ellipsoids [2,3,23–27] up to order 7 were sys-

tematically determined for selected aspect ratios. For two aspect ratios, in addition virial coefficients of order 8 are available [28].

In this paper, virial coefficients up to order 8 for the oblate geometries hard lenses and hard ellipsoids of revolution are systematically determined in dependence on their aspect ratio.

## II. VIRIAL COEFFICIENTS OF HARD SOLIDS

The virial coefficient of order  $i$  depends on the interactions in a cluster of  $i$  particles, which can for hard solids be exactly expressed in a pairwise additive representation,

$$V^{(i)} = \sum_i \sum_{j>i} V_{ij}, \quad (1)$$

where due to the absence of long-range interactions and the particles' impenetrability the pair interaction

$$V_{ij}(\mathbf{r}_{ij}, \hat{\mathbf{u}}_i, \hat{\mathbf{u}}_j) = \begin{cases} 0 & : r_{ij} \geq r_c(\hat{\mathbf{r}}_{ij}, \hat{\mathbf{u}}_i, \hat{\mathbf{u}}_j) \\ \infty & : r_{ij} < r_c(\hat{\mathbf{r}}_{ij}, \hat{\mathbf{u}}_i, \hat{\mathbf{u}}_j) \end{cases} \quad (2)$$

is either zero when both particles do not overlap or infinity when both particles intersect. At the contact distance  $r_c(\hat{\mathbf{r}}_{ij}, \hat{\mathbf{u}}_i, \hat{\mathbf{u}}_j)$ , two particles  $i$  and  $j$  touch when their orientation is given by the unit vectors  $\hat{\mathbf{u}}_i$  and  $\hat{\mathbf{u}}_j$  and the direction  $\hat{\mathbf{r}}_{ij} = \mathbf{r}_{ij}/r_{ij}$  of their center of mass distance vector  $\mathbf{r}_{ij}$ .

The Mayer  $f$  function  $f_{ij}(V_{ij}) = \exp(-V_{ij}/k_B T) - 1$  vanishes for a nonoverlap configuration and is  $f_{ij} = -1$  when particles  $i$  and  $j$  intersect, i.e.,

$$f_{ij}(\mathbf{r}_{ij}, \hat{\mathbf{u}}_i, \hat{\mathbf{u}}_j) = \begin{cases} 0 & : r_{ij} \geq r_c(\hat{\mathbf{r}}_{ij}, \hat{\mathbf{u}}_i, \hat{\mathbf{u}}_j) \\ -1 & : r_{ij} < r_c(\hat{\mathbf{r}}_{ij}, \hat{\mathbf{u}}_i, \hat{\mathbf{u}}_j) \end{cases}. \quad (3)$$

Since the energy is either zero or infinity, the Mayer  $f$  function and as a consequence the virial coefficients of hard body systems are independent of thermal energy  $k_B T$ .

The virial coefficient of order  $i$

$$B_i = -\frac{i-1}{i!} \sum_{G \in \mathbb{M}_i^+} S_G \quad (4)$$

\*joachim.wagner@uni-rostock.de



FIG. 1. Biconnected Mayer graphs with four nodes contributing to the fourth virial coefficient. The ten existing labeled graphs can be subdivided into three topological classes. The first node is represented by an open circle, at lower left, followed by three nodes labeled in counterclockwise direction.

is the sum of integrals  $S_G$  over products of Mayer  $f$  functions represented by the edges of graphs  $G$  in the set of biconnected or nonseparable labeled graphs  $\mathbb{M}_i^L$  with  $i$  nodes, called Mayer graphs. We have

$$B_2 = -\frac{1}{2V} \iint \langle f_{12} \rangle_{\hat{\mathbf{u}}_2} d^3 \mathbf{r}_1 d^3 \mathbf{r}_2 = -\frac{1}{2} \text{---} \text{---} \text{---} \quad (5a)$$

$$B_3 = -\frac{1}{3V} \iiint \langle f_{12} f_{13} f_{23} \rangle_{\hat{\mathbf{u}}_2, \hat{\mathbf{u}}_3} d^3 \mathbf{r}_1 d^3 \mathbf{r}_2 d^3 \mathbf{r}_3 = -\frac{1}{3} \triangle \quad (5b)$$

⋮

where  $\langle \dots \rangle_{\hat{\mathbf{u}}_2, \dots, \hat{\mathbf{u}}_i}$  indicates the average over the orientations of the second to  $i$ th particle, while the position  $\mathbf{r}_1$  and orientation  $\hat{\mathbf{u}}_1$  of the first particle determine the coordinate system.

While for the second and third virial coefficient, i.e., clusters of two or three particles, only one biconnected graph exists, already ten labeled graphs (Fig. 1) contribute to the fourth virial coefficient and 238 contribute to the fifth. The number of labeled biconnected graphs with  $i$  nodes can be found in Ref. [29].

The reformulation of Ree and Hoover [19,20,30] reduces the number of labeled graphs roughly to one third of the labeled Mayer graphs by introduction of a new type of bond  $e_{ij} = f_{ij} + 1$ . The resulting Ree-Hoover graphs are fully connected either by  $f$  bonds or  $e$  bonds as exemplarily shown for the fourth virial coefficient in Fig. 2. Since for hard solids we have

$$e_{ij}(\mathbf{r}_{ij}, \hat{\mathbf{u}}_i, \hat{\mathbf{u}}_j) = \begin{cases} 1 & : r_{ij} \geq r_c(\hat{\mathbf{r}}_{ij}, \hat{\mathbf{u}}_i, \hat{\mathbf{u}}_j) \\ 0 & : r_{ij} < r_c(\hat{\mathbf{r}}_{ij}, \hat{\mathbf{u}}_i, \hat{\mathbf{u}}_j) \end{cases} \quad (6)$$

$e_{ij}$  vanishes in the case of an intersection ( $f_{ij} = -1$ ) and  $f_{ij}$  vanishes for nonintersecting particles ( $e_{ij} = 1$ ). Hence, for a given configuration of overlaps and nonoverlaps only a single Ree-Hoover graph contributes to the integrand [31].

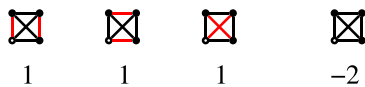


FIG. 2. Two topological classes of labeled Ree-Hoover graphs with four nodes and nonzero Ree-Hoover star contents contributing to the fourth virial coefficient exist. Ree-Hoover graphs are fully connected either via Mayer  $f$  bonds (black lines) or  $e$  bonds (red lines). The star contents as weighting factors result by replacing missing connections in Mayer graphs by a factor  $(e_{ij} - f_{ij}) = 1$ . Six remaining but noncontributing Ree-Hoover graphs with a single  $e$  bond are not displayed.

Using the Ree-Hoover reformulation, the virial coefficient of order  $i$  reads as

$$B_i = -\frac{i-1}{i!} \sum_{G \in \mathbb{R}_i^L} c_G S_G, \quad (7)$$

where  $\mathbb{R}_i^L$  is the set of labeled Ree-Hoover graphs with  $i$  vertices. The weighting factors  $c_G$ , called Ree-Hoover star contents, depend on the topology of the graphs in  $\mathbb{R}_i^L$ .

Since in a Ree-Hoover graph any combination of two nodes is either connected via a Mayer  $f$  bond or an  $e$  bond, its topology can be memory-efficiently represented as a binary number related to the upper triangle of its adjacency matrix, where  $i(i-1)/2$  bits are needed for a graph with  $i$  nodes. Herewith, Ree-Hoover graphs can be represented as ordinal numbers and thus be sorted. Based on the number of overlaps  $n_o$  and nonoverlaps  $i(i-1)/2 - n_o$ , a preclassification of possible graphs with a given number of  $f$  bonds is possible. In an ordered array of ordinal numbers, by means of a bisection search the single contributing graph and its star content can be identified very efficiently. The complexity of a bisection search scales as  $\log_2 N(i, n_o)$ , where  $N(i, n_o)$  is the cardinality of the set of Ree-Hoover graphs with  $i$  nodes and  $n_o$   $f$  bonds. Hence, a bisection search for virial coefficients of order 5 and higher is much faster than classical computation using integer arithmetic. The integrand resulting from such an identified configuration reads as  $(-1)^{n_o} c_G$ , since each  $f$  bond contributes as a factor of  $f_{ij} = -1$  for an overlap between particles  $i$  and  $j$  and each  $e$  bond as a factor of  $e_{ij} = 1$  in the case of a nonoverlap.

However, due to the highly increasing number of labeled Ree-Hoover diagrams, this method is restricted to virial coefficients up to order 9 using state-of-the-art hardware: for the binary representation of 21 286 987 064 labeled Ree-Hoover diagrams with nine nodes, where for each graph 5 bytes are necessary, roughly 100 GB of memory are required plus another 40 GB for the corresponding star contents. For even higher-order virial coefficients, the method of Wheatley is the fastest approach [32].

### A. Importance sampling

Calculating a virial coefficient of order  $i$  for an anisotropic solid of revolution requires numerical integration in  $5(i-1)$ -dimensional space, with three translational and two rotational degrees of freedom for each, except the first particle. Importance sampling can significantly improve the sampling of the configurational space where integrands are large. Singh and Kofke [33] proposed the Mayer-sampling method, where the acceptance of a trial is determined by the ratio of the system's integrand in subsequent configurations. Since in this approach the configuration space is no longer explored at constant sampling density, the comparison with a known integral of a reference system sampled at identical points of the configuration space is required in addition.

For a hard body system, i.e., a system with discontinuous  $f$  and  $e$  functions, which is sampled with a hard-body reference system of different shape, the situation can occur that the system's integrand is zero when the reference's integrand is nonzero. If the acceptance solely would be governed by the system's integrand, contributions to the reference integrand in

such configurations would not be sampled. Then, the accessible configuration space of the reference system would not be a subset of the system of interest’s accessible configuration space and importance sampling would fail. To facilitate that the union of accessible configuration spaces of both system of interest and reference is sampled exhaustively, the acceptance of a Monte Carlo trial in this paper is determined by the sum of moduli of sample and reference integrands. A weighting factor is adjusted during equilibration guaranteeing the same average moduli of system and reference integrands. Thus, both integrands contribute on average with equal weights to the acceptance of a trial.

**B. Trees as an intrinsic reference**

Since virial coefficients of hard spheres are the most accurate reference and the determination of overlaps of spheres is fast and simple, hard spheres scaled to the same volume as the particles of interest are an obvious reference system. Here, the virial coefficient of hard spheres or a diagram with known value can be used.

The efficiency of the Mayer-sampling method increases if the geometric shapes of the system of interest and reference system are as similar as possible. However, using anisotropic particles as a reference increases the numerical effort tremendously as a consequence of the orientation-dependent overlap problem. In addition, the accuracy of available virial coefficients is significantly smaller than that of hard sphere systems.

Both obstacles can be circumvented using trees with  $i$  nodes and  $i - 1$  Mayer  $f$  bonds as an intrinsic reference for the virial coefficient of order  $i$ . The number of labeled trees with  $i$  nodes is  $i^{i-2}$ . Since these graphs do not contain any leaves and all  $f$  bonds are connected via articulation points, they factorize to powers of the second virial coefficient. Each tree with  $i$  nodes and  $i - 1$  Mayer  $f$  bonds can be written as  $(-2B_2)^{i-1}$ . For convex hard bodies,  $B_2$  is analytically known employing the Isihara-Hadwiger theorem [9]. Even if the second virial coefficient is not analytically known in the case of concave bodies, it can numerically be determined with high accuracy.

If a set of trees with  $i$  nodes and  $i - 1$   $f$  bonds of cardinality  $N_T$  is used as an intrinsic reference, the value of the reference integral reads as

$$I_{\text{ref}} = N_T (-2B_2)^{i-1}. \tag{8}$$

With known overlaps and nonoverlaps in a given configuration, the reference integrand is the number of trees whose  $f$  bonds are a subset of the configuration’s nonzero  $f$  bonds. Although the number of trees does not increase as dramatically with the order of the virial coefficient as the number of Ree-Hoover diagrams, numerous trees with  $i$  nodes exist for high-order virial coefficients.

However, it is sufficient to use only those trees whose Mayer  $f$  bonds are most frequently a subset of the Ree-Hoover diagram’s  $f$  bonds. This is the case for the most branched trees, i.e., trees with nodes of highest order. In this paper, we used for the virial coefficient of order  $i$  trees with one node of order  $i - 1$  and  $i - 1$  nodes of order 1. This topological class consists of  $i$  labeled trees. For example,

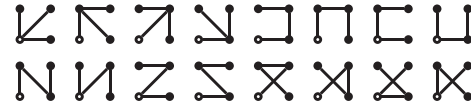


FIG. 3. Labeled trees with four nodes and three Mayer  $f$  bonds. Two topological classes with orders (3,1,1,1) and (2,2,1,1) can be distinguished. Since all Mayer  $f$  bonds of these trees are connected via articulation points, the value of each diagram is  $-8B_2^3$ .

to calculate the fourth virial coefficient, the first four trees displayed in Fig. 3 are used.

**III. OVERLAP CRITERIA FOR HARD ELLIPSOIDS AND HARD LENSES**

**A. Ellipsoid**

Overlaps between ellipsoids can be identified using the algorithm proposed by Perram and Wertheim [34]. Since a numerical maximization is involved, the algorithm can be optimized employing a Newton-Raphson maximization instead of the Brent maximization originally proposed by the authors.

**B. Lens**

A lens is the section of two spheres with radii  $R_0$  whose centers are less than their diameter  $2R_0$  apart from each other. The radius  $R_0$  of spheres generating a lens with equatorial radius  $r_{\text{eq}}$  and aspect ratio  $\nu$  is

$$R_0 = \frac{\nu^2 + 1}{2\nu} r_{\text{eq}}, \tag{9}$$

as illustrated in Fig. 4.

The equator at  $z = 0$  is a two-dimensional singularity of surface curvature for  $\nu < 1$ . In contrast, the surface curvature of ellipsoids is completely continuous. In the limits  $z \rightarrow 0^+$  and  $z \rightarrow 0^-$ , the tangents enclose the critical angle  $\vartheta_{\text{crit}} = \arccos[(1 - \nu^2)/(1 + \nu^2)]$  with the lens’s equatorial plane.

Choosing  $r_{\text{eq}} = 1$ , two lenses  $i$  and  $j$  possibly intersect with a center to center distance  $r_{ij} < 2$ . With  $r_{ij} < 2\nu$ , they definitely intersect. For  $2\nu < r_{ij} < 2$ , an intersection is possible

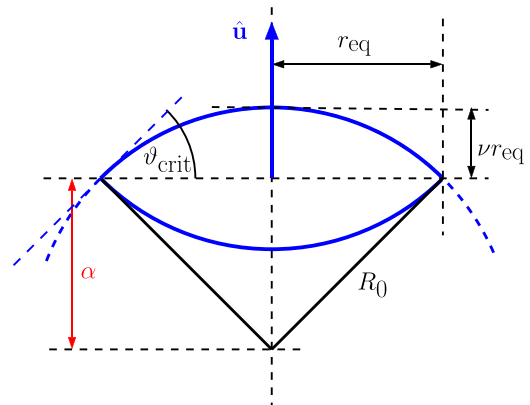


FIG. 4. A lens is the section of two spheres with center to center distance less than their diameter  $2R_0$ , where  $r_{\text{eq}}$  is the lens’s equatorial radius and  $\nu$  is its aspect ratio. Its orientation is denoted by the unit vector  $\hat{\mathbf{u}}$  perpendicular to its equatorial plane.

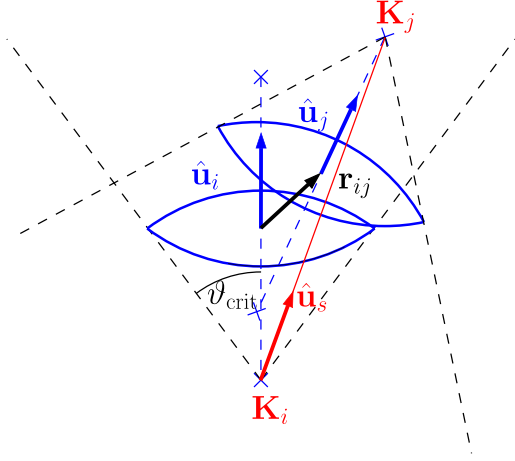


FIG. 5. Undercritically inclined lenses with  $|\hat{\mathbf{u}}_i \cdot \hat{\mathbf{u}}_s| > \zeta$  and  $|\hat{\mathbf{u}}_j \cdot \hat{\mathbf{u}}_s| > \zeta$ , where  $\zeta = (1 - v^2)/(1 + v^2)$  denotes the cosine of the critical angle  $\vartheta_{\text{crit}}$ . Undercritically inclined lenses do not touch at a singularity of surface curvature at their equators.

if a generating sphere of lens  $i$  intersects with a generating sphere of lens  $j$ .

Let  $\hat{\mathbf{u}}_i$  and  $\hat{\mathbf{u}}_j$  be the orientations of lenses  $i$  and  $j$  with each vector being perpendicular to its equatorial plane. Without loss of generality, we can choose  $\mathbf{r}_i = \mathbf{0}$  and  $\hat{\mathbf{u}}_i$  defining the  $z$  direction of the coordinate system. Thus, the generating spheres of a lens with center of mass  $\mathbf{r}_i$  are located at

$$\mathbf{c}_{i\pm} = \mathbf{r}_i \pm \alpha \hat{\mathbf{u}}_i, \quad (10)$$

where  $\alpha = R_0 - \nu r_{\text{eq}}$  is the distance of the sphere center to the lens's equatorial plane.

An intersection of two lenses  $i$  and  $j$  is possible if at least one of four possible distances  $\|\mathbf{c}_{j\pm} - \mathbf{c}_{i\pm}\| < 2R_0$  is smaller than the diameter  $2R_0$  of generating spheres. An intersection, however, occurs if and only if at least one point of the generating spheres' intersection simultaneously is inside both lenses  $i$  and  $j$ .

An intersection can be proven or excluded by the following tests. The closest surface to surface distance between two nonintersecting lenses occurs between the most distant generating spheres of both lenses. In a first step, let us look for the maximum of

$$d_{\text{max}} = \max \|\mathbf{r}_{ij} \pm \alpha \hat{\mathbf{u}}_j \mp \alpha \hat{\mathbf{u}}_i\|. \quad (11)$$

Let  $\mathbf{K}_i$  and  $\mathbf{K}_j$  be the centers of generating spheres of lens  $i$  and lens  $j$  with the distance  $d_{\text{max}} = \|\mathbf{K}_j - \mathbf{K}_i\|$ . Let further  $\hat{\mathbf{u}}_s = (\mathbf{K}_j - \mathbf{K}_i)/\|\mathbf{K}_j - \mathbf{K}_i\|$  be the direction of the distance vector and  $\zeta = (1 - v^2)/(1 + v^2)$  the cosine of the critical angle  $\vartheta_{\text{crit}}$ . If simultaneously  $|\hat{\mathbf{u}}_i \cdot \hat{\mathbf{u}}_s| > \zeta$  and  $|\hat{\mathbf{u}}_j \cdot \hat{\mathbf{u}}_s| > \zeta$ ,  $\mathbf{K}_j$  is in the critical cone of lens  $i$  and  $\mathbf{K}_i$  is in the critical cone of lens  $j$ . Then, both lenses are undercritically inclined to each other (Fig. 5). In this case, the equatorial circles of both lenses are not in their section.

Undercritically inclined lenses intersect if  $\mathbf{K}_j + R_0 \hat{\mathbf{u}}_s$  is inside lens  $j$  or  $\mathbf{K}_j - R_0 \hat{\mathbf{u}}_s$  is inside lens  $i$  and otherwise not. Hence, an intersection is excluded for undercritically inclined lenses if  $d_{\text{max}} > 2R_0$ .

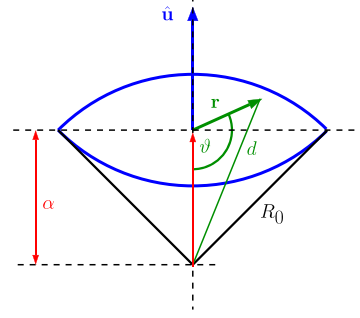


FIG. 6. A point  $\mathbf{r}$  is inside a lens if its distance to the generating sphere's center is smaller than the radius  $R_0$  of the generating sphere.

For overcritically inclined lenses, we need to check if the nearest point of lens  $i$ 's equator to  $\mathbf{K}_j$  is inside lens  $j$  or the nearest point of lens  $j$ 's equator to  $\mathbf{K}_i$  is inside lens  $i$ . The two points of interest are

$$\mathbf{P}_i = \mathbf{r}_i + r_{\text{eq}} \frac{\hat{\mathbf{u}}_i \times [(\mathbf{K}_j - \mathbf{r}_i) \times \hat{\mathbf{u}}_i]}{\|\hat{\mathbf{u}}_i \times [(\mathbf{K}_j - \mathbf{r}_i) \times \hat{\mathbf{u}}_i]\|} \quad (12a)$$

and

$$\mathbf{P}_j = \mathbf{r}_j + r_{\text{eq}} \frac{\hat{\mathbf{u}}_j \times [(\mathbf{K}_i - \mathbf{r}_j) \times \hat{\mathbf{u}}_j]}{\|\hat{\mathbf{u}}_j \times [(\mathbf{K}_i - \mathbf{r}_j) \times \hat{\mathbf{u}}_j]\|}. \quad (12b)$$

Finally, we have to check if the equator circles of both lenses intersect. This is only possible if the intersection line of the planes containing the equators of the respective lenses intersects both equator circles. The sufficient condition for an overlap of lenses is fulfilled when both obtained line segments overlap. This is the case when the intervals  $[x_1^{(i)}, x_2^{(i)}]$  and  $[x_1^{(j)}, x_2^{(j)}]$  overlap, where  $x_1^{(i)}$  and  $x_2^{(i)}$  are solutions of  $\mathbf{r}^T \cdot \mathbf{r} = 1$  and  $x_1^{(j)}$  and  $x_2^{(j)}$  are solutions of  $(\mathbf{r} - \mathbf{r}_j)^T \cdot (\mathbf{r} - \mathbf{r}_j) = 1$  under the constraint  $\mathbf{r}^T \cdot \hat{\mathbf{u}}_j = 0$  with  $\mathbf{r} = (x, y, 0)$  in the coordinate system defined by lens  $i$ .

The required tests of whether a point of interest  $\mathbf{r}$  is inside or outside a lens centered at  $\mathbf{c}$  with orientation  $\hat{\mathbf{u}}$  can be done as follows: Let us again without loss of generality choose  $\mathbf{c} = \mathbf{0}$ . A point is inside a lens if its distance to the generating sphere's center is smaller than  $R_0$  (Fig. 6). With  $\vartheta = \pi - \arccos(\hat{\mathbf{r}} \cdot \hat{\mathbf{u}})$ , where  $\hat{\mathbf{r}}$  and  $\hat{\mathbf{u}}$  are unit vectors indicating the direction of  $\mathbf{r}$  and lens orientation  $\hat{\mathbf{u}}$ , we obtain

$$\begin{aligned} d^2 &= \alpha^2 + r^2 - 2\alpha r \cos[\pi - \arccos(\hat{\mathbf{r}} \cdot \hat{\mathbf{u}})] \\ &= \alpha^2 + r^2 + 2\alpha \mathbf{r} \cdot \hat{\mathbf{u}}. \end{aligned} \quad (13)$$

Should  $\mathbf{r}$  be located at the lower hemilens when  $\mathbf{r} \cdot \hat{\mathbf{u}} < 0$ , the edge  $d$  of a triangle containing the sphere center above the lens's equatorial plane as a corner decides if  $\mathbf{r}$  is inside or outside the lens. Hence,  $\mathbf{r}$  is inside the lens whenever

$$\alpha^2 + r^2 + 2\alpha |\mathbf{r} \cdot \hat{\mathbf{u}}| < R_0^2. \quad (14)$$

As the above described overlap algorithm does not contain any iterative numerical step, checking overlaps of lenses is significantly faster than checking overlaps of ellipsoids.

The comparison of second virial coefficients obtained from numerical integration employing the above described overlap algorithm with the analytical result proves its reliability:



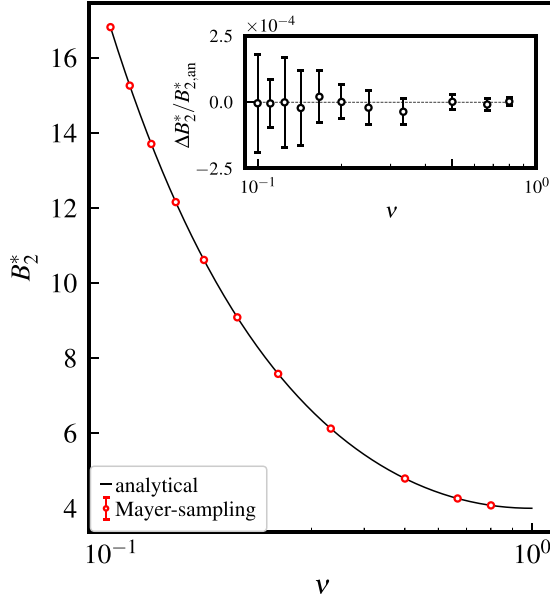


FIG. 7. Comparison of reduced second virial coefficients  $B_2^* = B_2/V_P$  of hard lenses obtained numerically with the respective analytical values. The numerical integration is performed via Mayer sampling using hard spheres as a reference, where the spheres are scaled to obtain a sphere volume identical to the lens volume. In the inset, relative deviations  $\Delta B_2^* = (B_2^* - B_{2,an}^*)/B_{2,an}^*$  from the analytical values are displayed.

within experimental uncertainties, results from Mayer sampling agree with the analytical values (Fig. 7). Here, the second virial coefficient of hard spheres with volume identical to the lens volume is used as a reference.

#### IV. RESULTS

Despite the geometric similarity between oblate ellipsoids of revolution and lenses, the latter shape differs from ellipsoids by a two-dimensional equatorial discontinuity in its surface curvature. In addition, at the same equatorial radius  $r_{eq}$  and aspect ratio  $\nu$ , both volume and surface of lenses are smaller than those of ellipsoids. As a consequence of the discontinuity of curvature, however, for  $\nu < 1$  the strongly increasing mean curvature radius of lenses overcompensates the drop of volume and surface: with decreasing aspect ratio

$\nu$ , the second virial coefficient of lenses increasingly exceeds that of oblate uniaxial ellipsoids [9].

As in the limit  $\nu \rightarrow 1$  both geometries approach a sphere, the comparison of virial coefficients of lenses and ellipsoids with aspect ratio  $\nu = 1$  with literature data of hard spheres is a test for the reliability of our algorithm optimized for hard anisotropic shapes. The excellent accordance of our data with reference values from [35] can be seen from the compilation in Table I. Since the scope of this paper is a systematic, aspect ratio dependent comparison of both geometries' virial coefficients, the data for the limiting case of spheres obtained by comparatively short simulations do not reflect a principal limitation of our algorithm in terms of accuracy.

Reduced virial coefficients  $\tilde{B}_i = B_i/B_2^{i-1}$  calculated by means of the above described algorithm are compiled for oblate ellipsoids of revolution in Table II and for lenses in Table III. For both investigated geometries, the dependence of virial coefficients on the aspect ratio decreases with increasing order of the virial coefficient.

Our data for hard ellipsoids are in excellent agreement with data previously published from order 3 to 7 in Ref. [27]. The accuracy, however, could be improved by our algorithm. For moderately anisotropic particles, eighth-order virial coefficients could be accessed with acceptable accuracy. Since for highly anisotropic shapes small rotations influence the number of overlaps in a cluster drastically, exhaustive sampling of the configuration space is hampered in the case of large anisotropy. Hereby, the fluctuations of virial coefficients during Mayer sampling significantly increase, leading to uncertainties in the magnitude of the observable itself. As a consequence, for  $\nu \leq 1/7$  only a limit for the eighth virial coefficients' moduli could be obtained. In Ref. [28] two virial coefficients of order 8 for ellipsoids of moderate aspect ratio are reported which could not be reproduced in terms of either value or uncertainty. As reported in Ref. [36], only a subset of possible diagrams was utilized for the calculation of these two virial coefficients.

For three-dimensional hard, convex bodies, Boublík [37] proposed the quantity  $\alpha^{-1}$ , which is proportional to the mutual excluded volume, as a geometric measure, leading to comparatively simple correlations to the reduced virial coefficients  $\tilde{B}_i = B_i/B_2^{i-1}$ . In three dimensions, for convex shapes the excess part of the mutual excluded volume can, employing the Isihara-Hadwiger theorem [38] with the volume  $V_P$ , the

TABLE I. Second to eighth virial coefficients of hard spheres [35] and hard ellipsoids of revolution and lenses with aspect ratio  $\nu = 1$  (this paper). In the limit  $\nu \rightarrow 1^-$ , both anisotropic shapes approach a sphere.  $\Delta^{(ell)} = (B_i^{*(ell)} - B_i^{*(sph)})/B_i^{*(sph)}$  and  $\Delta^{(lens)} = (B_i^{*(lens)} - B_i^{*(sph)})/B_i^{*(sph)}$  are relative deviations from literature data of hard spheres. The values in parentheses indicate the standard deviations of at least eight independent runs, each with  $2 \times 10^{10}$  Monte Carlo steps.

	Spheres	Ellipsoids ( $\nu = 1$ )	$\Delta^{(ell)}$	Lenses ( $\nu = 1$ )	$\Delta^{(lens)}$
$B_2^*$	4				
$B_3^*$	10	10.0002(3)	$2.0 \times 10^{-5}$	9.9999(7)	$-1.0 \times 10^{-5}$
$B_4^*$	18.3647684...	18.365(2)	$1.3 \times 10^{-5}$	18.364(1)	$-4.2 \times 10^{-5}$
$B_5^*$	28.224437(15)	28.224(7)	$-2.9 \times 10^{-5}$	28.23(1)	$2.0 \times 10^{-4}$
$B_6^*$	39.81523(10)	39.80(3)	$-3.8 \times 10^{-4}$	39.81(2)	$-1.3 \times 10^{-4}$
$B_7^*$	53.34208(49)	53.3(1)	$-1.1 \times 10^{-3}$	53.3(2)	$-7.9 \times 10^{-4}$
$B_8^*$	68.5285(28)	68.6(6)	$1.0 \times 10^{-3}$	68.5(4)	$-4.2 \times 10^{-4}$

TABLE II. Reduced third to eighth virial coefficients  $\tilde{B}_i = B_i/B_2^{i-1}$  of oblate, hard ellipsoids of revolution. The values in parentheses indicate the standard deviations of at least eight independent runs, each with  $2 \times 10^{10}$  Monte Carlo steps.

$\nu$	$\tilde{B}_3$	$\tilde{B}_4$	$\tilde{B}_5$	$\tilde{B}_6$	$\tilde{B}_7$	$\tilde{B}_8$
1	0.624998(46)	0.286935(17)	0.110260(38)	0.038874(21)	0.013079(41)	0.004183(25)
4/5	0.621429(22)	0.281755(18)	0.106449(41)	0.036954(19)	0.012247(26)	0.004693(210)
2/3	0.613817(30)	0.270539(32)	0.098223(25)	0.032895(41)	0.010623(30)	0.003342(76)
1/2	0.595464(35)	0.243124(25)	0.078313(43)	0.023378(35)	0.007081(13)	0.002078(68)
1/3	0.562854(29)	0.194102(25)	0.043556(36)	0.008142(77)	0.002143(38)	0.000657(90)
1/4	0.539669(37)	0.159003(35)	0.019600(32)	-0.001217(79)	-0.000142(54)	0.000248(70)
1/5	0.523263(35)	0.134251(29)	0.003238(25)	-0.006938(111)	-0.001224(43)	0.000118(95)
1/6	0.511319(17)	0.116317(31)	-0.008217(46)	-0.010571(94)	-0.001819(26)	0.000111(87)
1/7	0.502348(27)	0.102906(26)	-0.016542(35)	-0.012959(179)	-0.001915(55)	0.000077(250)
1/8	0.495413(32)	0.092570(28)	-0.022834(50)	-0.014566(54)	-0.001993(76)	-0.000016(187)
1/9	0.489884(32)	0.084401(24)	-0.027656(49)	-0.015730(100)	-0.001882(109)	0.000043(270)
1/10	0.485403(26)	0.077811(24)	-0.031481(34)	-0.016480(72)	-0.001853(22)	0.000064(268)

surface  $S_P$ , and the mean radius of curvature  $\tilde{R}$ , be written as

$$\alpha = \frac{B_2 - V_P}{3V_P} = \frac{B_2^* - 1}{3} = \frac{S_P \tilde{R}_P}{3V_P}, \quad (15)$$

where the factor  $1/3$  guarantees  $0 < \alpha^{-1} \leq 1$  with  $\alpha^{-1} = 1$  being the upper limit for hard spheres. The geometric measures  $V_P$ ,  $S_P$ , and  $\tilde{R}_P$  for hard lenses and oblate ellipsoids of revolution are provided in the Appendix.

At first approximation, for both investigated shapes an identical dependence of reduced virial coefficients  $\tilde{B}_i$  on the geometric measure  $\alpha^{-1}$  emerges as visible in Figs. 8 and 9.

For reduced virial coefficients  $\tilde{B}_3$ ,  $\tilde{B}_4$ , and  $\tilde{B}_5$ , a nearly linear dependence is obtained. For the higher orders  $\tilde{B}_6$ ,  $\tilde{B}_7$ , and  $\tilde{B}_8$ , a generalized, nonlinear dependence is visible, which can be reasonably approximated by parabolas (Fig. 9). The limitation of this parabolic approximation can be identified by deviations of this approximation to the data exceeding their uncertainties. This is also reflected by the optimum parameters of least-squares fits to a polynomial,

$$\tilde{B}_i(\alpha^{-1}) = a_{0,i} + a_{1,i}\alpha^{-1} + a_{2,i}\alpha^{-2}, \quad (16)$$

where the intercepts  $a_{0,i}$  are quite similar for lenses and ellipsoids. The curvatures  $a_{2,i}$  of ellipsoids, however, exceed those

of lenses, while the linear coefficients  $a_{1,i}$  of lenses are larger than those of ellipsoids (Fig. 10 and Table IV).

## V. EQUATION OF STATE

With the virial series the real gas factor reads as

$$\begin{aligned} Z &= \frac{p}{k_B T \varrho} = 1 + B_2 \varrho + B_3 \varrho^2 + \dots \\ &= 1 + \sum_{i=2}^{\infty} B_i \varrho^{i-1}, \end{aligned} \quad (17)$$

where  $k_B T$  denotes the thermal energy and  $\varrho$  denotes the particle number density. With the volume  $V_P$  of a hard body, the volume fraction can be written as  $\varphi = \varrho V_P$ . Employing reduced virial coefficients  $B_i^* = B_i/V_P^{i-1}$ , the real gas factor can be reformulated as

$$Z = \frac{pV_P}{k_B T \varphi} = 1 + \sum_{i=2}^{\infty} B_i^* \varphi^{i-1}. \quad (18)$$

The reduced virial coefficients  $B_i^*$  of hard spheres can for  $i \geq 2$  be approximated by the Carnahan-Starling series as  $B_i^* \approx i^2 + i - 2$  [39]. The reason why this approximation

 TABLE III. Reduced third to eighth virial coefficients  $\tilde{B}_i = B_i/B_2^{i-1}$  of hard lenses. The values in parentheses indicate the standard deviations of at least eight independent runs, each with  $2 \times 10^{10}$  Monte Carlo steps.

$\nu$	$\tilde{B}_3$	$\tilde{B}_4$	$\tilde{B}_5$	$\tilde{B}_6$	$\tilde{B}_7$	$\tilde{B}_8$
1	0.625012(21)	0.286957(28)	0.110249(29)	0.038867(27)	0.013009(27)	0.004187(36)
4/5	0.620911(35)	0.280841(33)	0.105628(46)	0.036445(43)	0.011946(17)	0.003786(77)
2/3	0.611414(43)	0.266666(21)	0.095071(30)	0.031080(41)	0.009732(20)	0.002932(98)
1/2	0.588039(11)	0.231810(35)	0.069868(22)	0.019239(39)	0.005436(39)	0.001468(86)
1/3	0.549095(31)	0.173328(22)	0.029403(43)	0.002691(24)	0.000916(73)	0.000571(80)
1/4	0.524367(29)	0.135765(19)	0.004218(31)	-0.006408(50)	-0.000861(145)	0.000340(158)
1/5	0.508397(29)	0.111646(18)	-0.011454(37)	-0.011596(25)	-0.001656(42)	0.000360(170)
1/6	0.497563(31)	0.095327(39)	-0.021663(34)	-0.014575(49)	-0.001943(147)	0.000287(82)
1/7	0.489793(40)	0.083754(40)	-0.028697(47)	-0.016477(92)	-0.002043(122)	0.000198(214)
1/8	0.483953(38)	0.075178(33)	-0.033683(55)	-0.017556(69)	-0.002093(83)	0.000221(197)
1/9	0.479431(44)	0.068622(38)	-0.037424(42)	-0.018290(75)	-0.002058(101)	0.000230(226)
1/10	0.475858(18)	0.063396(28)	-0.040296(65)	-0.018748(47)	-0.001815(104)	0.000257(120)

TABLE IV. Optimum parameters  $a_{0,i}$ ,  $a_{1,i}$ , and  $a_{2,i}$  of Eq. (16) describing the dependence of the reduced virial coefficients  $\tilde{B}_i$  on the inverse excess part of the excluded volume  $\alpha^{-1}$  for orders  $i = 3$  to 8. The values in parentheses indicate the standard deviations of the parameters determined via weighted least squares fits.

$i$	Ellipsoid			Lens		
	$a_0$	$a_1$	$a_2$	$a_0$	$a_1$	$a_2$
3	0.44274(17)	0.17047(63)	0.01157(50)	0.43979(96)	0.1877(43)	-0.0011(39)
4	0.01352(32)	0.2561(12)	0.01730(95)	0.0088(19)	0.2804(72)	-0.0014(56)
5	-0.06831(55)	0.13820(20)	0.0405(15)	-0.0739(17)	0.1629(67)	0.0224(55)
6	-0.02316(31)	0.0141(11)	0.04794(85)	-0.02576(75)	0.0246(27)	0.0401(21)
7	0.00112(8)	-0.01986(31)	0.03174(26)	0.00027(25)	-0.01616(94)	0.02882(72)
8	0.00252(49)	-0.0115(15)	0.0132(11)	0.00184(35)	-0.0090(13)	0.01130(99)

works surprisingly well is still not understood [40]. Using the obvious condition  $0 \leq \varphi < 1$ , for the geometric series

$$\sum_{i=2}^{\infty} (i^2 + i - 2)\varphi^{i-1} = \frac{2\varphi(2 - \varphi)}{(1 - \varphi)^3}, \quad (19)$$

a closed expression is obtained. Herewith, the Carnahan-Starling real gas factor

$$Z = 1 + \frac{2\varphi(2 - \varphi)}{(1 - \varphi)^3} \quad (20)$$

of hard spheres results.

Introducing reduced virial coefficients normalized to powers of the second virial coefficients  $\tilde{B}_i = B_i^*/(B_2^*)^{i-1}$ , the expression

$$Z = 1 + \sum_{i=2}^{\infty} \tilde{B}_i (B_2^*)^{i-1} \quad (21)$$

is obtained for the real gas factor  $Z$ . Note that for a convergent sum in Eq. (21)  $B_2^*\varphi < 1$  is not necessarily required in addition to  $\varphi < 1$ .

For the equation of state of hard anisotropic solids, the known virial coefficients of the respective geometry can be used in combination with an approximation of higher virial coefficients by the Carnahan-Starling series. With analytically known second-order and numerically determined third- to eighth-order virial coefficients using

$$\sum_{i=9}^{\infty} (i^2 + i - 2)\varphi^{i-1} = \frac{2\varphi^8(35\varphi^2 - 78\varphi + 44)}{(1 - \varphi)^3}, \quad (22)$$

we can express the real gas factor  $Z$  as

$$Z = 1 + \sum_{i=2}^8 \tilde{B}_i (B_2^*)^{i-1} + \frac{2\varphi^8(35\varphi^2 - 78\varphi + 44)}{(1 - \varphi)^3}. \quad (23)$$

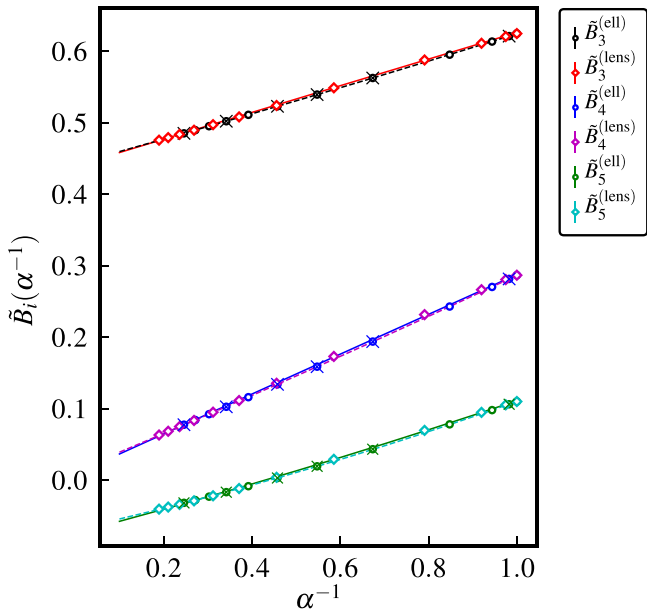


FIG. 8. Reduced virial coefficients  $\tilde{B}_3$ ,  $\tilde{B}_4$ , and  $\tilde{B}_5$  of hard lenses and hard ellipsoids of revolution as a function of the excluded volume's inverse excess part  $\alpha^{-1}$ . The crosses represent data from [27]. The lines are least-squares fits of lens and ellipsoid data to parabolas [Eq. (16)].

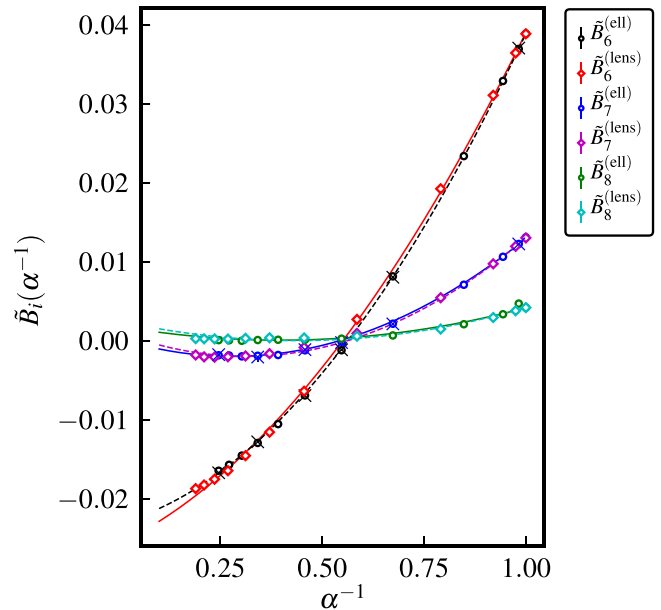


FIG. 9. Reduced virial coefficients  $\tilde{B}_6$ ,  $\tilde{B}_7$ , and  $\tilde{B}_8$  of hard lenses and hard ellipsoids of revolution as a function of the excluded volume's inverse excess part  $\alpha^{-1}$ . The lines are least-squares fits of lens and ellipsoid data to parabolas [Eq. (16)]. The crosses represent data from [27].

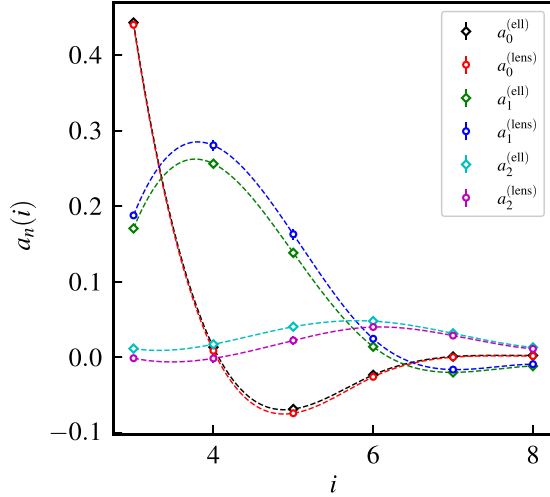


FIG. 10. Optimum parameters  $a_{0,i}$ ,  $a_{1,i}$ , and  $a_{2,i}$  of Eq. (16) describing the dependence of the reduced virial coefficients  $\tilde{B}_i$  on the inverse excess part of the excluded volume  $\alpha^{-1}$  for orders  $i = 3$  to 8. The dotted lines are cubic splines as a guide to the eye.

Employing Eq. (16), we obtain

$$Z = 1 + \frac{2\varphi^8(35\varphi^2 - 78\varphi + 44)}{(1 - \varphi)^3} + B_2^* \varphi + \sum_{i=3}^8 (a_{0,i} + a_{1,i}\alpha^{-1} + a_{2,i}\alpha^{-2})(B_2^*\varphi)^{i-1} \quad (24)$$

as an approximative interpolation for the real gas factor of hard, oblate ellipsoids of revolution and lenses. Since the slope of  $\tilde{B}_i$  versus  $\alpha^{-1}$  decreases systematically with increasing order of the virial coefficients and presumably approaches zero (Fig. 9), approximating orders  $i \geq 9$  of so far unknown virial coefficients of anisotropic particles by those of hard spheres [Eq. (22)] is a suitable approach.

The Parsons approach [26,41] approximates high-order virial coefficients of anisotropic hard bodies by rescaling Carnahan-Starling virial coefficients by a factor of  $B_2^*(\nu)/B_2^{*(\text{HS})}$ , where  $B_2^{*(\text{HS})} = 4$  denotes the reduced second virial coefficient of hard spheres. While negative virial coefficients of highly anisotropic particles cannot be approximated in an adequate way by this approach, our numerical data for eighth-order virial coefficients are reasonably described by this approach. Probably, rescaling the contribution of even higher virial coefficients given by Eq. (22) in this way could improve the real gas factor in Eq. (24).

The effect of increasing the order of the virial expansion on the real gas factor is exemplarily shown in Fig. 11 for ellipsoids and Fig. 12 for lenses, each with an aspect ratio of  $\nu = 1/4$ . By comparison, the influence of more negative sixth- and seventh-order virial coefficients of lenses becomes evident.

In the following, we investigate for selected aspect ratios the dependence of the real gas factor  $Z$  on the volume fraction. Here, we focus on the interval of confidence of the real gas factor given by Eq. (23) derived from uncertainties of virial coefficients from order 3 to 8 and the reliability of the interpolation approach [Eq. (24)].

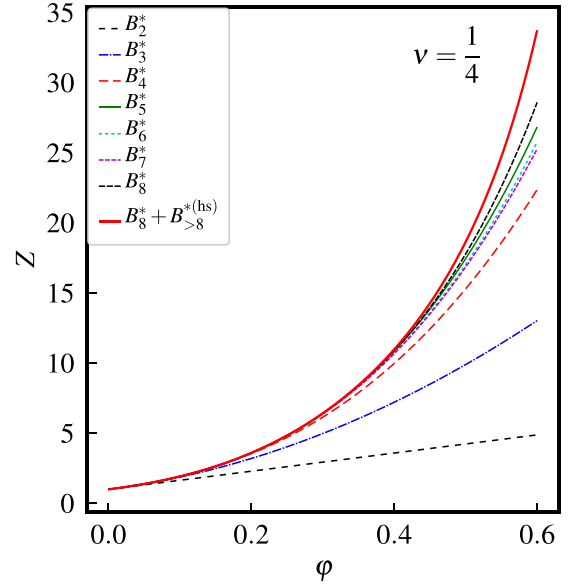


FIG. 11. Real gas factor  $Z$  of ellipsoids with aspect ratio  $\nu = 1/4$  for different orders of the virial series. Indicated is the highest-order term contributing to  $Z$ . The thick solid line includes the contribution of higher-order virial coefficients approximated by the Carnahan-Starling series, Eq. (22).

For less anisotropic particles, Eq. (24) excellently describes real gas factors up to the maximum random packing fraction (Fig. 13), which can exceed that of hard spheres [42]. With increasing anisotropy, at least for small and moderate volume fractions, a reasonable approximation within the accuracy of available virial coefficients is possible (Figs. 14

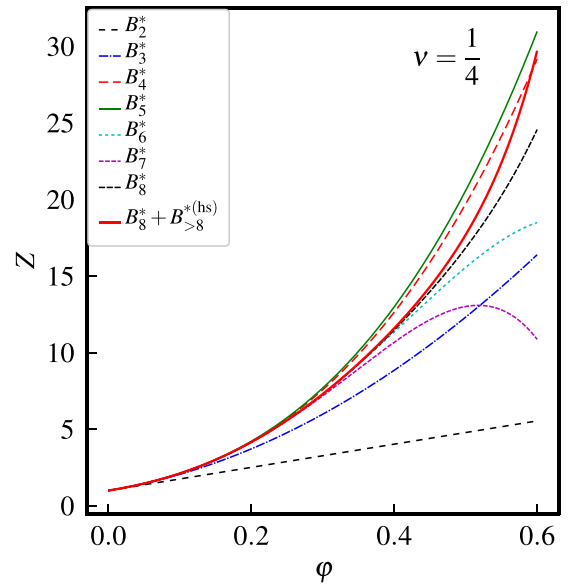


FIG. 12. Real gas factor  $Z$  of lenses with aspect ratio  $\nu = 1/4$  for different orders of virial series. Again, the highest-order term contributing to  $Z$  is indicated, and for the thick solid line the contribution of higher-order virial coefficients approximated by the Carnahan-Starling series, Eq. (22), is included.



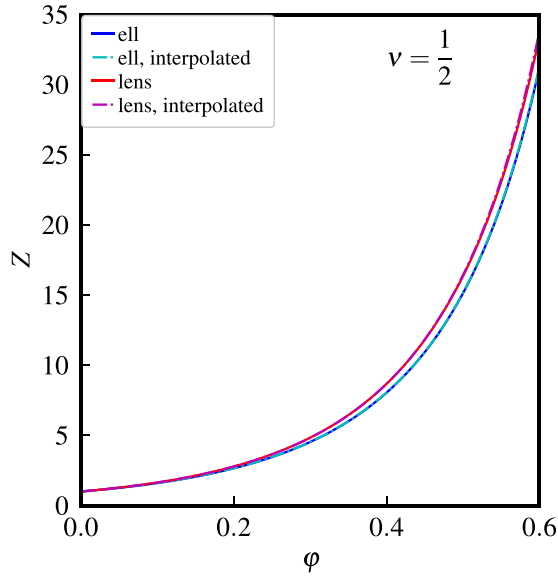


FIG. 13. Real gas factor  $Z$  for ellipsoids of revolution and lenses with aspect ratio  $\nu = 1/2$  as a function of volume fraction  $\phi$ . Displayed are real gas factors resulting from Eq. (23), where analytically known second virial coefficients  $B_2^*$  and numerically determined virial coefficients of order 3 to 8 are used. The contributions of higher-order virial coefficients are approximated by virial coefficients obtained from the Carnahan-Starling series, leading to Eq. (22). The real gas factors calculated by the interpolation [Eq. (24)], displayed as dashed lines, agree excellently with those obtained from virial coefficients calculated for aspect ratio  $\nu = 1/2$ . The uncertainties of the real gas factors are less than the width of the solid lines.

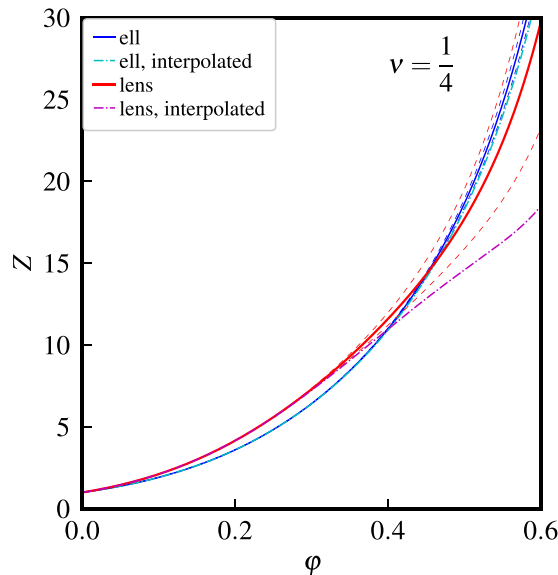


FIG. 14. Real gas factor  $Z$  for ellipsoids of revolution and lenses with aspect ratio  $\nu = 1/4$  as a function of volume fraction  $\phi$ . The real gas factors obtained from virial coefficients for aspect ratio  $\nu = 1/4$  are represented as solid lines; those from interpolation [Eq. (24)] are represented as dashed-dotted lines. The uncertainties are indicated by thin dashed lines. While for ellipsoids the interpolation is nearly up to  $\phi = 0.6$  within the uncertainty of the real gas factor, the interpolation deviates in the case of lenses for  $\phi \gtrsim 0.4$ .

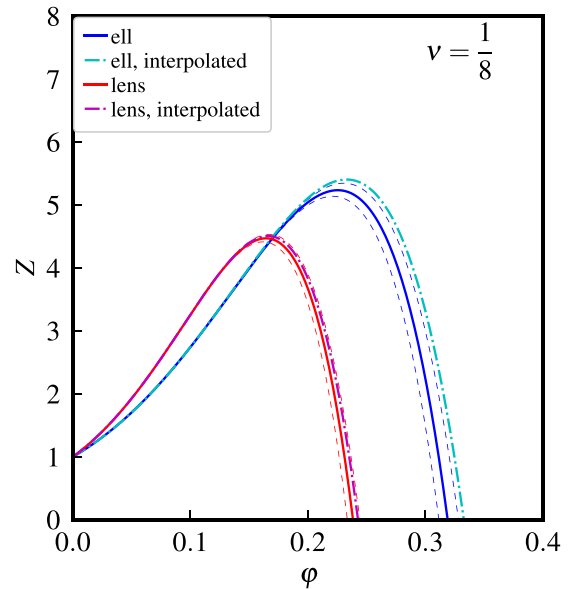


FIG. 15. Real gas factor  $Z$  for ellipsoids of revolution and lenses with aspect ratio  $\nu = 1/8$  as a function of volume fraction  $\phi$ . Possible reasons for the decrease of real gas factor  $Z$  with increasing volume fraction  $\phi$  are the truncation of the virial series or an isotropic-nematic phase transition, which occurs for hard lenses at volume fractions significantly smaller than for hard ellipsoids of revolution. Again, the real gas factors resulting from virial coefficients for aspect ratio  $\nu = 1/8$  are displayed as solid lines and the interpolation according to Eq. (24) is displayed as dashed-dotted lines.

and 15). For higher volume fractions, the uncertainty of the real gas factor  $Z$ , however, increases significantly.

For highly anisotropic shapes, a decreasing real gas factor with increasing volume fraction  $\phi$  could either be related to an isotropic-nematic phase transition or insufficient approximation of higher-order virial coefficients by those of spheres. The critical volume fraction for this transition is in the case of lenses significantly smaller than in the case of hard ellipsoids: while the maximum real gas factor at an aspect ratio  $\nu = 1/8$  is found at a volume fraction  $\phi \approx 0.23$  for hard ellipsoids, in the case of hard lenses the maximum real gas factor occurs at  $\phi \approx 0.17$ .

### VI. DISCUSSION

The numerical effort for the calculation of virial coefficients increases dramatically with the order  $i$  of the respective virial coefficient. One reason is the number  $i(i-1)/2$  of pair interactions in an  $i$  cluster roughly quadratically increasing with order  $i$ . Much more severe is the superexponential increase of labeled graphs that need to be considered.

With an optimized algorithm based on bisection search of an ordered representation of Ree-Hoover graphs, where for hard bodies only a single graph contributes at a given configuration to the virial coefficients, the value of this single contributing graph can rapidly be determined. The CPU time needed to determine virial coefficients up to order 8 increases in first approximation logarithmically with the order of the virial coefficients.

Since rotational degrees of freedom dramatically increase the dimensionality of configuration space compared to spherically symmetric systems, a highly efficient numerical integration algorithm is required. Importance sampling algorithms such as Mayer sampling efficiently explore the configuration space in regions where integrands contribute significantly. Since with this method the configuration space is no longer explored with uniform sampling density, a known reference integral has to be sampled simultaneously.

The efficiency and accuracy of importance sampling increase when the reference system and system of interest are as similar as possible. The approach of Singh and Kofke [33] to use a known virial coefficient or at least one or more graphs contributing to a known virial coefficient requires the determination of pair interactions both in the system of interest and reference system. For anisotropic hard solids, the determination of orientation-dependent contact distances is numerically demanding. Hence, identifying overlaps and nonoverlaps both in the system of interest and reference system requires considerable computing resources.

The numerical effort can drastically be reduced using a known integral of the same system instead which depends on already determined overlaps and nonoverlaps. Here, trees as graphs are a suitable reference, whose integrals can be written as powers of the second virial coefficient, which is for convex bodies analytically known. However, this approach is not limited to convex bodies, since the second virial coefficients of concave objects are numerically accessible with high accuracy, too. The increase of virial coefficients' uncertainties related to not exactly known reference integrals is still acceptable. Statistical fluctuations of virial coefficients during Mayer-sampling Monte Carlo runs using the same system as a reference are considerably smaller than those using a geometry of similar shape.

Since in the the limit  $\nu \rightarrow 1^-$  ellipsoids and lenses approach spheres, a comparison with highly accurate literature data of spheres can be used to validate our algorithm. The relative deviations  $\Delta^{(\text{ell})}$  and  $\Delta^{(\text{lens})}$  smaller than  $10^{-3}$  even for the eighth virial coefficients indicate the reliability of this algorithm optimized for hard, anisotropic particles. Deviations of virial coefficients independently determined employing the contact algorithms for ellipsoids and lenses in the limit  $\nu \rightarrow 1^-$  from literature data of hard spheres are significantly smaller than our error estimates. This indicates realistic confidence intervals.

Using this improved algorithm, virial coefficients of order 3 to 8 of differently shaped, oblate solids of revolution were obtained systematically with high accuracy for a large range of aspect ratios.

The accuracy of available virial coefficients of ellipsoids could be improved. Simultaneously, the thus obtained data validate the reliability of our optimized algorithm. In addition, hitherto unknown virial coefficients of hard lenses from order 3 to 8 are calculated.

Interestingly, normalizing higher virial coefficients  $\tilde{B}_i(\nu) = B_i(\nu)/B_2(\nu)^{i-1}$  to powers of the second virial coefficients  $B_2(\nu)$  leads in first approximation to a universal dependence on the inverse reduced excess part  $\alpha^{-1}$  of their mutual excluded volume. As the ratio of mutual excluded volume to the particle volume  $V_P$  is the reduced second virial

coefficient  $B_2^*(\nu) = B_2(\nu)/V_P$ , the excess part of the excluded volume,  $B_2^*(\nu) - 1$ , is solely related to the second virial coefficient.

Reduced virial coefficients  $\tilde{B}_i$  from order 3 to 5 show a nearly linear dependence on the inverse excess part of the excluded volume  $\alpha^{-1}$ , while from order 6 to 8 a slight non-linearity occurs, which, however, can be described reasonably by a second-order polynomial. This in first approximation universal behavior of reduced virial coefficients  $\tilde{B}_i$  of lenses and ellipsoids of revolution suggests that the entire dependence of the virial series of hard solids on the particle geometry is essentially reflected by the second virial coefficient. With this approximation, the equation of state for such particles can be formulated in a closed expression.

However, the comparison of further geometric shapes including prolate solids of revolution such as ellipsoids, spherocylinders, or spindles is a pending task deciding if this behavior is universal for hard solids.

#### ACKNOWLEDGMENT

P.M. gratefully acknowledges financial support by the Universität Rostock within the Ph.D. scholarship program.

#### APPENDIX: ANALYTICAL SECOND VIRIAL COEFFICIENTS OF OBLATE, HARD ELLIPSOIDS OF REVOLUTION AND LENSES

The second virial coefficient of convex hard solids is analytically accessible from the geometric measures volume, surface, and mean radius of curvature by means of the Isihara-Hadwiger theorem [9,38,43,44]. The reduced second virial coefficients of convex hard bodies are

$$B_i^* = 1 + \frac{S_P \tilde{R}_P}{V_P}, \quad (\text{A1})$$

where  $S_P$  is the surface,  $\tilde{R}_P$  is the mean radius of curvature, and  $V_P$  is the volume of the particle. These geometric measures read for oblate ellipsoids of revolution as

$$S_P^{(\text{ell})} = \frac{2\pi r_{\text{eq}}^2}{\sqrt{1-\nu^2}} \left[ \nu^2 \ln \left( \frac{1 + \sqrt{1-\nu^2}}{\nu} \right) + \sqrt{1-\nu^2} \right], \quad (\text{A2a})$$

$$\tilde{R}_P^{(\text{ell})} = \frac{\nu r_{\text{eq}}}{2} + \frac{r_{\text{eq}}}{2\sqrt{1-\nu^2}} \arctan \left( \frac{\sqrt{1-\nu^2}}{\nu} \right), \quad (\text{A2b})$$

$$V_P^{(\text{ell})} = \frac{4\pi}{3} \nu r_{\text{eq}}^3, \quad (\text{A2c})$$

and for lenses as

$$S_P^{(\text{lens})} = 2\pi r_{\text{eq}}^2 (1 + \nu^2), \quad (\text{A3a})$$

$$\tilde{R}_P^{(\text{lens})} = \nu r_{\text{eq}} + \frac{r_{\text{eq}}}{2} \arctan \left( \frac{1 - \nu^2}{2\nu} \right), \quad (\text{A3b})$$

$$V_P^{(\text{lens})} = \pi r_{\text{eq}}^3 \left( \nu + \frac{\nu^3}{3} \right), \quad (\text{A3c})$$

where  $r_{\text{eq}}$  and  $\nu$  denote the particles' equatorial radius and aspect ratio.

- [1] L. Onsager, *Ann. NY Acad. Sci.* **51**, 627 (1949).
- [2] D. Frenkel, B. M. Mulder, and J. P. McTague, *Phys. Rev. Lett.* **52**, 287 (1984).
- [3] B. Mulder and D. Frenkel, *Mol. Phys.* **55**, 1193 (1985).
- [4] G. Odriozola, *J. Chem. Phys.* **136**, 134505 (2012).
- [5] G. Bautista-Carbajal, A. Moncho-Jordá, and G. Odriozola, *J. Chem. Phys.* **138**, 064501 (2013).
- [6] J. Vieillard-Baron, *Mol. Phys.* **28**, 809 (1974).
- [7] P. Bolhuis and D. Frenkel, *J. Chem. Phys.* **106**, 666 (1997).
- [8] J. A. C. Veerman and D. Frenkel, *Phys. Rev. A* **41**, 3237 (1990).
- [9] E. Herold, R. Hellmann, and J. Wagner, *J. Chem. Phys.* **147**, 204102 (2017).
- [10] G. Cinacchi and S. Torquato, *J. Chem. Phys.* **143**, 224506 (2015).
- [11] G. Cinacchi and S. Torquato, *Soft Matter* **14**, 8205 (2018).
- [12] G. Cinacchi and S. Torquato, *Phys. Rev. E* **100**, 062902 (2019).
- [13] J. D. van der Waals, *Proc. K. Ned. Akad. Wet.* **1**, 138 (1899).
- [14] B. Jäger, *Sitzungsber. Akad. Wiss. Wien, Math.-Naturwiss. Kl., Abt. 2A* **105**, 15 (1896).
- [15] L. Boltzmann, *Sitzungsber. Akad. Wiss. Wien, Math.-Naturwiss. Kl., Abt. 2A* **105**, 695 (1896).
- [16] L. Boltzmann, *Proc. K. Ned. Akad. Wet.* **1**, 398 (1899).
- [17] H. Kamerlingh Onnes, *Proc. K. Ned. Akad. Wet.* **4**, 125 (1902).
- [18] M. N. Rosenbluth and A. W. Rosenbluth, *J. Chem. Phys.* **22**, 881 (1954).
- [19] F. H. Ree and W. G. Hoover, *J. Chem. Phys.* **40**, 939 (1964).
- [20] F. H. Ree and W. G. Hoover, *J. Chem. Phys.* **46**, 4181 (1967).
- [21] P. A. Monson and M. Rigby, *Mol. Phys.* **35**, 1337 (1978).
- [22] D. Frenkel, *J. Phys. Chem.* **91**, 4912 (1987).
- [23] W. Cooney, S. Thompson, and K. Gubbins, *Mol. Phys.* **66**, 1269 (1989).
- [24] M. Rigby, *Mol. Phys.* **66**, 1261 (1989).
- [25] J. A. C. Veerman and D. Frenkel, *Phys. Rev. A* **45**, 5632 (1992).
- [26] C. Vega, *Mol. Phys.* **92**, 651 (1997).
- [27] X.-M. You, A. Y. Vlasov, and A. J. Masters, *J. Chem. Phys.* **123**, 034510 (2005).
- [28] A. Y. Vlasov, X.-M. You, and A. J. Masters, *Mol. Phys.* **100**, 3313 (2002).
- [29] The On-Line Encyclopedia of Integer Sequences, <https://oeis.org>, Sequence A013922, accessed in 2021.
- [30] F. H. Ree and W. G. Hoover, *J. Chem. Phys.* **41**, 1635 (1964).
- [31] C. Zhang and B. M. Pettitt, *Mol. Phys.* **112**, 1427 (2014).
- [32] R. J. Wheatley, *Phys. Rev. Lett.* **110**, 200601 (2013).
- [33] J. K. Singh and D. A. Kofke, *Phys. Rev. Lett.* **92**, 220601 (2004).
- [34] J. W. Perram and M. Wertheim, *J. Comp. Phys.* **58**, 409 (1985).
- [35] A. J. Schultz and D. A. Kofke, *Phys. Rev. E* **90**, 023301 (2014).
- [36] S. Labík, J. Kolafa, and A. Malijevský, *Phys. Rev. E* **71**, 021105 (2005).
- [37] T. Boublík, *Mol. Phys.* **27**, 1415 (1974).
- [38] H. Hadwiger, *Experientia* **7**, 395 (1951).
- [39] N. F. Carnahan and K. E. Starling, *J. Chem. Phys.* **51**, 635 (1969).
- [40] Y. Song, E. A. Mason, and R. M. Stratt, *J. Phys. Chem.* **93**, 6916 (1989).
- [41] J. D. Parsons, *Phys. Rev. A* **19**, 1225 (1979).
- [42] A. Baule, R. Mari, L. Bo, L. Portal, and H. A. Makse, *Nat. Commun.* **4**, 2194 (2013).
- [43] A. Isihara, *J. Chem. Phys.* **18**, 1446 (1950).
- [44] A. Isihara and T. Hayashida, *J. Phys. Soc. Jpn.* **6**, 40 (1951).